Control jet-slender body performance characteristics at hypersonic speeds

by
K Kontis

College of Aeronautics
Cranfield University
Cranfield
Bedfordshire MK43 0AL
England

Control jet-slender body performance characteristics at hypersonic speeds

by
K Kontis

College of Aeronautics
Cranfield University
Cranfield
Bedfordshire MK43 0AL
England

CONTROL JET-SLENDER BODY PERFORMANCE CHARACTERISTICS AT HYPERSONIC SPEEDS

K Kontis[+]

College of Aeronautics, Cranfield University
Cranfield, Bedfordshire, UK MK43 0AL

"The views expressed herein are those of the author/s alone and do not necessarily represent those of the university"

ABSTRACT

The jet control effectiveness of a 5° semi-angle cone has been tested at hypersonic speeds. The study has been carried out in the Cranfield hypersonic gun tunnel facility at a Mach number of 8.2, and a Reynolds number based on base diameter of 3.788×10^5. Under those conditions, the initial boundary layer in the absence of the jet was laminar. The jet was injected normal to the cone surface at sonic speed. Both sharp and blunted cones were used. The jet/flowfield interaction, including boundary-layer separation and its influence upon aerodynamic coefficients was determined. Pressure and force measurements were made in the incidence range of -15° to 15°. The forces were measured with a 3-component balance equipped with semi-conductor strain gauges. The flow structure was studied using high speed schlieren photography. Jet penetration distances have been compared with theoretical estimates.

NOTATION

A	area
A	axial force
A_b	cross section area of equivalent penetration model
C	Chapman-Rubesin constant
CA	axial force coefficient
Cd	nose drag coefficient
Cm	pitching moment coefficient
CN	normal force coefficient
C_p	pressure coefficient
$C_{p,max}$	stagnation pressure coefficient
d	diameter
F_i	interaction force
F_j	jet thrust
$F_{j,v}$	vacuum thrust of a sonic jet
h	penetration height
K	amplification factor
L	total cone length
L_{sep}	separation distance
M	Mach number
M	pitching moment
N	normal force
P	pressure
Re/m	unit Reynolds number
x'	distance along the cone surface measure from jet nozzle
Xcp	axial centre of pressure

α	angle of attack (^{o})
γ	ratio of specific heats
δ_e	equivalent half cone angle
δ	cone semi-angle
κ_ε	bluntness parameter
ϕ	flow momentum flux
Φ	ray angle of sharp cone
χ	viscous interaction parameter
	$(= M_\infty^3 \sqrt{\dfrac{C}{Re_x}})$

Subscripts

b	at base
e	at jet exit
j	jet flow property
n	nose
o	total value
w	wall
1	condition behind a shock
2	condition ahead separation
∞	freestream

INTRODUCTION

From the early 1950s, engineering interest in the flowfield created by sonic gaseous jet exhausting normal to a surface into an external flow has been the subject of experimental investigations. At about that time secondary fluid injection was proposed as an attractive method of controlling the flight path or attitude of a space vehicle or missile, by augmentation or supplantation of the aerodynamic control forces. Such a system is very beneficial in situations where conventional aerodynamic surfaces cannot function properly, because either due to the low density of the medium or the considerable aerodynamic heating effects. The Space Shuttle is a current example of the application of jet control for orbital flight manoeuvring. Even in cases where the interaction force becomes very small, like in rarefied flows, the jet thrust is still available for control.

Taylor (1954) studied first the interaction of a two-dimensional jet of air issuing from a long narrow slit set at right angles to the flow. Since then, a number of investigators have published work dealing with secondary flowfield interactions. Investigators like **Orth and Lasky (1971), Zukoski and Spaid (1964), Charwat and Allegre (1965)**, to mention a few, have done serious research in order to clarify the salient features of such interaction processes. However, most of them have restricted themselves to flows over flat plates, and freestream Mach numbers up to 5 or 6. While extensive studies have been undertaken with regard to the technique of thrust vectoring, limited attention has been paid to the hypersonic interaction as a means of attitude control. The complexity of flowfields created by jets interacting with external crossflows is such that the present understanding of them relies heavily on experimental data.

EXPERIMENTAL SET-UP

1. Models

The general geometrical characteristics of the slender cone configurations are shown in figure 1. The ratio of the nose to the base radius (bluntness), expressed as a percentage figure, was 33.445 %. The models used for schlieren observations were equipped with a sigle jet hole. Pressure models were equipped with tappings along the jet meridian. The injectant gas (air) was fed at room temperature via a plenum chamber which was located directly beneath the nozzle, inside the models, sealed by an "O" ring to prevent jet air leakage.

The force model's air feed system used dual injection ports located in the horizontal axis plane of the model. This set-up imposed yaw moments due to differences in feed pipe pressure. For the balance, the coupling between the normal force and the pitching moment components to yaw moment components was negligible. The pressure feed employed coiled tubes. These coils allowed movement similar to a spring and thus reduced the coupling forces between the jet feed system and the model. The objective was to make them as light as possible, and place the centre of gravity of the cones as near the sensing elements of the balance. A small moment arm reduces the influence of the inertial forces to the readings (and especially to the pitching moment output) and increases the accuracy.

2. Gun tunnel facility

All the experiments were conducted in the College of Aeronautics 8" gun tunnel. The tests were carried out with air as the freestream gas. A axi-symmetric contoured nozzle provided a uniform flow of $M_\infty = 8.2$ with useful test jet diameter of 152mm. The tunnel is equipped with a high speed sigle-pass schlieren system. This uses a high intensity microsecond duration argon spark source to illuminate density gradients in the flow. Pressure measurements were carried out using Kulite XCS-190 series pressure transducers. All measurements were taken during the interval of 25 to 45 msec. The tunnel provided a useful run time of 25 msec and an overall run time of about 80 msec.

3. Force balance

The force balance is based on the design used by **Opatowski (1971)**. It is a three component strain balance, each equipped with 4 silicon gauges. With the balance in its normal position, it was taken as convention that a positive (backward) axial force should produce an decrease in output voltage, a positive (upward) normal force and a positive (nose up) pitching moment both produce an increase in output voltage.

4. FFT analysis and digital filtering of force measurements

During the running of the tunnel, the working section is subjected to severe mechanical oscillations. Due to its mass inertia, these oscillations produce damped harmonic oscillations. The output signal was analysed using a fast fourier transform analysis (FFT) package. Digital filters were designed, in order to remove the main natural frequency of the balance and the three dynamic modes each dominant in the corresponding measured output, together with their coupling modes and harmonics components.

REVIEW OF LITERATURE

1. Shock-wave/boundary layer interaction

In high Mach and low Reynolds number regimes, the shockwave-boundary layer interaction can significally modify the aerodynamic performance of a surface. In many cases, this type of interaction generates adverse pressure gradients of sufficient strength to cause boundary layer separation, leading to formation of a recirculatory flow region at the wall, and can significally modify the displacement surface. At the separation point, the wall velocity gradient and therefore the skin friction is zero. The inviscid pressure rise due to the shock feeds forward through the subsonic sub-layer of the boundary layer causing the low momentum fluid near the wall to slow down. This results in thickening of the velocity boundary layer.

2. Entropy layer effects

The introduction of bluntness modifies the aerodynamic properties of the flow over a slender body from that with an equivalent sharp leading edge. The bow shockwave stands off from the leading edge and is highly curved, with an increase in strength near the leading edge. These characteristics give rise to gradients in flow properties normal to the cone surface. The most important feature of the flow is that the streamtubes crossing the shock near the nose suffer a large entropy rise and then expand rapidly downstream. This entropy layer is a region of high temperature and low density. The result is total pressure losses due to the bow shock and lower local Mach numbers in this layer than the freestream. The density gradients associated with the entropy layer disguise the gradients associated with the boundary layer, thus making the identification of separation of the flow very difficult. It influences the local flow conditions for a large distance downstream. This entropy layer is eventually swallowed by the boundary layer.

3. Effect of nose bluntness on separation

Simpkins (1968) found that the introduction of nose bluntness promotes separation. He did an experimental comparison of the interaction between a two-dimensional underexpanded jet and the hypersonic flow over a sharp and a blunt cone of semi-angle five degrees at a freestream Mach number of thirteen, with laminar boundary layer. **Vermeulen and Simeonides (1992)** also found the promotion of separation due to bluntness from pressure distribution measurements. On the other hand, other researchers, like **Townsend (1966), Coet, Delery and Chantez (1992)** in their experiments on flat plates, found appreciable reduction of the separated flow region of laminar boundary layers due to the introduction of nose bluntness.

Holden (1975) indicates, that leading edge bluntness may have a strong effect on the viscous-inviscid interaction and the occurrence and extent of flow separation. The extent of the laminar separated region is governed by the viscous bluntness interaction parameter $\chi_c / \kappa_c^{\frac{2}{3}}$, where

$$\kappa_c = M_\infty^3 Cd \frac{\gamma-1}{\gamma+1}(\frac{d_n}{x})$$

is the bluntness parameter and

$$\chi_c = \frac{\gamma-1}{\gamma+1}[0.664+1.73(\frac{T_w}{T_o})]\chi$$

Hence the viscous bluntness interaction parameter takes into account the relative effects of Mach number and Reynolds number on the interaction. For $0.1 \leq \chi_{\varepsilon}/\kappa_{\varepsilon}^{\frac{2}{3}} \leq 0.5$, leading edge bluntness promotes separation, while for $\chi_{\varepsilon}/\kappa_{\varepsilon}^{\frac{2}{3}} \leq 0.1$, the leading edge bluntness reduces the extent of boundary layer separation.

Small bluntness cause reduction in the local surface Mach number which exceeds in influence a decrease in the Reynolds number, and therefore an increase in the size of the separation region is observed. On the other hand, at larger bluntnesses, the changes in local Mach number and Reynolds number are smaller, and hence the effect of the strong favourable pressure gradient has more influence.

ANALYTICAL MODELS

1. Blast wave analogy

Near the nose, the distribution of flow properties in the shock layer is similar to that predicted by blast-wave theory while many nose radii downstream, the distribution is essentially conical except for the thin entropy layer. As the entropy layer thins with increasing axial distance, the surface pressure expands below, and then approaches, asymptotically, the sharp-cone pressure. In accordance with the second-approximation form of the pressure equation which evolves from Blast-wave theory, it can be shown (**Van Hise**) that the actual equation governing the pressure distribution is given by

$$\frac{P}{P_{\infty}} = 0.06\{\frac{M_{\infty}^{2}Cd^{0.5}}{x/d_{n}}\} + 0.55 \text{ , for air}$$

The nose drag coefficient is obtained by integrating the modified Newtonian flow pressure distribution over the hemispherical nose. For the modified Newtonian flow, Cd=0.964.

Using **Brower's** tables, the pressure coefficient on the surface of a 5 degree semi-angle sharp cone was extrapolated, ($C_{p_{2}} = 0.01969$). Hence,

$$\frac{P}{P_{\infty}} = 1 + \frac{Cp_{2}q_{\infty}}{P_{\infty}} = 1 + \frac{Cp_{2}\gamma_{\infty}M_{\infty}^{2}}{2} = 1.93$$

Substituting $\frac{d_{n}}{x} = 0.0936$ (it corresponds to the location of jet orifice), Cd=0.964, $M_{\infty} = 8.2$, $T_{w} = 296$ K, $T_{o} = 1290$ K, $\gamma_{x} = 1.4$, $C \approx 1$ and Reynolds number based on the base diameter, 3.788×10^{5} into Holden's equations, it was found that $\chi_{\varepsilon}/\kappa_{\varepsilon}^{\frac{2}{3}} = 0.0387 \leq 0.1$. Since the viscous bluntness interaction parameter is less than 0.1, the leading edge bluntness is expected to reduce the extent of boundary layer separation and to make the boundary layer transition occur further upstream in comparison with an equivalent sharp cone configuration.

2. Estimation of the local surface Mach number

The local Mach number value corresponds to the undisturbed region ahead of separation, at the edge of the boundary layer.

a) Blunt cone

The flow was assumed to expand isentropically from the reservoir to the freestream ahead of the bow shock. The flow between that region and the tip of the cone was not isentropic. In that case the normal shock relations were used. After manipulation and substitution of $M_{\infty} \sin\theta$ (where θ is the shock angle) for M_{∞} to include the oblique shock case, together with the assumption that the conditions along a streamline downstream of the leading edge shock are isentropic, it was derived that the local Mach number can be calculated by

$$M_{2} = \sqrt{\frac{2}{\gamma_{x}-1}\{(\frac{P_{ol}}{P_{2}})^{\frac{\gamma-1}{\gamma}}-1\}}$$

b) Sharp cone

1) $\alpha = 0^{o}$

Using the tables of **Brower** for compressible flow, the local surface Mach number was extrapolated, hence $M_{2} = 7.39$.

4

2) $\alpha < 0^o$

High and Blick (1964) analysis is based on the concept of the equivalent cone (a right circular cone at zero incidence having the same freestream Mach number and a half cone angle equal to the angle between the freestream Mach number vector and the ray line on the cone under examination). δ_e was calculated by

$$\delta_e = \sin^{-1}(\sin\delta\cos\alpha + \cos\delta\sin\alpha\cos\Phi)$$

with $\Phi=0^o$ at the bottom ray line and 180° at the top ray line. The local Mach number was calculated, for δ_e evaluated at Φ equal to 180 degrees. For K<1,

$$M_2 = M_\infty \cos\delta_e (1 - \frac{\sin\delta_e}{M_\infty})^{\frac{1}{2}} \{[1+e^{-1.52K}][1+(\frac{K}{2})^2]\}^{-\frac{1}{2}}$$

if $K \geq 1$,

$$M_2 = M_\infty \cos\delta_e (1 - \frac{\sin\delta_e}{M_\infty})^{\frac{1}{2}} (1 + 0.35K^{\frac{3}{2}})^{-\frac{1}{2}}$$

where K is the hypersonic similarity parameter $M_\infty \sin\delta_e$.

3) $\alpha > 0^o$

A Prandtl-Meyer expansion was assumed from the freestream conditions to the surface values. Since the flow is isentropic the usual relations hold. Hence

$$M_2 = \sqrt{\frac{2}{\gamma_\infty - 1}\{\frac{(1+\frac{\gamma_\infty-1}{2}M_\infty^2)}{(\frac{P_2}{P_\infty})^{\frac{\gamma_\infty-1}{\gamma_\infty}}} - 1\}}$$

3. Estimation of the aerodynamic coefficients - No jet
a) Blunt body configuration

Trimmer (1966) equations were solved as a function of angle of attack. The pitching-moment coefficient was calculated from the following relationship,

$$Cm = CN(\frac{Xcp}{l_b})$$

b)Sharp body configuration

Wells and Armstrong (1961) closed-form expressions were used to calculate CN and CA. The pitching moment coefficient was calculated by

$$Cm = \frac{L}{3l_b}(1 - 2\tan^2\delta)CN$$

The centre of pressure was determined by

$$Xcp = l_b \frac{Cm}{CN}$$

RESULTS AND DISCUSSION

1. Description of the jet flowfield

The jet flowfield interaction region is shown in figure 2. Figure 3a shows the jet only without external flow. The experiments were conducted at $Re\infty/mm=9.05\times10^6$ with a jet reservoir pressure of $P_{oj}=110$ psia. The freestream pressure ($P\infty$) was taken to be 0.137 psia, giving a ratio $P_{oj}/P\infty \approx 800$. Due to the relatively high Mach number and the low Reynolds number, the initial boundary layer on the surface of the cones, in the absence of the jet, was laminar.

The jet plume presents an obstacle to the external flow, which causes a strong shock which separates the boundary layer upstream of the jet. In contrast to the two-dimensional situation in which the entire external flow must go over the jet-induced obstruction, the flow can go around the three-dimensional jet. The flowfield near the separation point is controlled by the interaction between the resultant free shear layer and the external stream. This free-interaction region is insensitive to the disturbance which creates the separation. The location of the separation point is a function of the

the jet efflux. In the forward region of the separated flowfield, the pressure distribution is controlled by the free-interaction process. The distributions in the neighbourhood of the disturbance, are dependent on the phenomena creating the separation and are closely related to the details of the jet characteristics.

As a result of high pressures downstream of the shock and mixing between the two streams, the jet is turned in the direction of the external flow. A three-dimensional shock structure forms in the jet plume as it is turned, bounded by a three-dimensional mixing layer. The wave angle of this shock was equal to or greater than that of a shock giving maximum flow deflection. Some of the high pressure external air behind this shock flows downstream causing the high pressure ridge in front of the jet. From this high pressure region, the external air flows radially outward along the surface of the cone, expanding to lower pressures. Finally this expanding reverse flow is terminated by a shock system. The location of this shock system corresponds with the forward edge of the region lying just ahead of the pressure ridge. As the reverse flow continues outward from the jet it turns toward the downstream direction. A continuous flow of high pressure external air enters the separation region behind the strong shock, to replace this separated flow escaping downstream. The geometry of the downstream separated region implies a component of velocity normal to the wall upstream of the reattachment. The recompression shock is required to turn the flow parallel to the wall.

The mixing layer surrounds the plume and reattaches to the body downstream. In the region where the mixing layer surrounding the jet reattaches to the body, a set of vortices forms in the jet wake rotating around each other, figure 3b.

An important feature of interest is the strong shock which terminates the supersonic region of the jet (often referred to often as the Mach disc or normal shock). The Mach disk is dish-shaped and parallel to the exit plane. In the presence of a hypersonic external flow, the jet is partially turned before the Mach disk is reached. The shock structure within an underexpanded jet which interacts with an external flow is quite similar to the shock structure within an underexpanded jet exhausting into a quiescent medium for at least a few exit diameters from the exit plane. A shear layer surrounds the jet at the exit. In order to satisfy the boundary conditions, at least two counter-rotating vortices must present within the upstream separated region.

2. Parameters for data presentation

a) In considering the general phenomenon of jet interaction, it is most appropriate to define the control parameters of the problem. The ratio of jet to undisturbed flow momentum flux was used, defined by

$$\frac{\phi_j}{\phi_\infty} = \frac{P_{oj} \gamma_j M_j^2 d_{jet}^2}{P_\infty \gamma_\infty M_\infty^2 l_b^2}$$

The surface pressure and the local Mach number ahead of separation seems to be important control parameters, since as the incidence or the nose-tip geometry changes the pressure distribution of the region, together with the Mach number ahead of the separation are varying. This ratio reduces to (for $l_b = 41.86$ mm, $d_{jet} = 2$ mm, and $\gamma_j = \gamma_\infty$)

$$\frac{\phi_j}{\phi_2} = \frac{0.0478^2 P_{oj}}{P_2 M_2^2} \approx \frac{P_{oj}}{P_2 M_2^2}$$

b) The interaction force developed upstream and downstream of a three dimensional, normal, sonic jet can be represented in the form of amplification factor, K. The amplification factor is defined as the jet thrust plus the interaction force generated both upstream and downstream of the jet, normalised by the thrust of the sonic jet.

$$K = \frac{F_i + F_j}{F_{j,v}}$$

3. Schlieren visualisation studies
3.1 Effect of bluntness

It was found (figure 4) that the introduction of nose bluntness, although it effectively increases the jet strength by reducing the local surface pressure ahead of the separation region, causes a delay in separation. The reduced lengths of the separated regions are also evident from the pressure distributions (figure 5).

Holden's theory predicted reduction of separation (for 0 degree incidence). The viscous bluntness interaction parameter should be at all incidences less or equal to 0.1. A decrease of the transition Reynolds number and a reduction of the local Reynolds number will effect the location of transition, relative to the sharp cone model. That implies, that the boundary layer becomes turbulent earlier on the blunt cone. It is known that turbulent layers are more resistant to adverse pressure gradients, which are the cause of separation.

As the viscous bluntness interaction parameter goes closer to 0.1, the delay effect of nose bluntness on the separated flow region gets smaller. From schlieren pictures it was observed (figure 4), that although the separation region is smaller on the blunt cone for all incidences, the separation distances differ only a little from the sharp cone results, at negative incidences. The difference is increasing as the incidence is increasing as well. That means that the viscous bluntness interaction parameter value is higher in the negative incidences and the delay effect of nose bluntness

6

is much smaller. This observation is connected with the local surface Mach number, which is smaller at negative incidences and causes K_ε to decrease.

The boundary-layer edge becomes less visible for the blunt-cone configuration as the incidence increasing, and it becomes totally invisible at incidences 10 and 15 degrees. This is because of the very low density of the flow near the body decreases the sensitivity of the schlieren system and because the highly curved shock wave produces strong density gradients throughout the entire flow field that tend to obscure the density gradients at the boundary layer.

3.2 Effect of incidence

The introduction of incidence modifies substantially the undisturbed surface pressure distribution. On the windward side of the cone, the surface pressures ahead the interaction region are larger, therefore, the jet penetration is reduced while on the leeward side the pressures are lower, the penetration is increased, hence the separation length is increased as well. Data collected from the schlieren pictures for incidence effects shows that the separation length increases as the incidence becomes more positive.

A large separated region is created which exhibits very strong three-dimensional interactions. The separation three-dimensional oblique shock can be seen emanating from the base of the cones. Evidence was found on schlieren pictures (at negative incidence only) of the existence of a reattachment shock downstream of the jet. The oscillation of the bow wave ahead of the jet is apparent in all schlieren pictures and it is believed to be associated with the unstable characteristics of the jet/separated shear layer interaction.

3.3 Separation length correlation

A correlation of the length of separated flow along the jet meridian for the two cone configurations is shown in figure 6. The correlation of the data in the absence of any Reynolds number factors suggests that small changes in unit Reynolds number do not affect length of the separated flow. The data correlates as

$$\frac{L_{sep}}{d_j} = 0.762 \left[\frac{P_{oj}}{P_2 M_2^2} \right]^{1.633} B$$

where B=1 for the sharp cone and

$$B = 0.241 \left[\frac{P_2 M_2^2}{P_{oj}} \right]^{0.461} \text{ for the blunt cone.}$$

The correlation suggests that the length of the separated flow region increases with an increase in the jet to undisturbed flow surface value pressure ratio and decrease in the local Mach number ahead separation. The factor B represents the effect of bluntness on separation. However, it is important to note that the range of variables was limited and more data is required.

3.4 Equivalent penetration model

The schlieren pictures of the shock patterns produced by the jet injection, are reminiscent of the flow around a circular protubing from a solid surface. The modified equation of **Zukoski et al** was used and its results were compared with the experimental findings. It can be shown for

$$\gamma_j = \gamma_2 = \gamma_\infty = 1.4$$

$$\left(\frac{A_b}{A_j}\right)^{\frac{1}{2}} = \frac{2.275}{M_2} \left(\frac{P_{oj}}{P_2 C_{p,\max}}\right)^{\frac{1}{2}} [1 - (\frac{P_2}{P_{oj}})^{\frac{2}{7}}]^{\frac{1}{4}}$$

$$C_{p,\max} = \left(\frac{8.933 M_2^2}{7 M_2^2 - 1}\right)^{\frac{5}{2}} - \frac{1}{0.7 M_2^2}$$

If a quarter sphere-half cylinder model is assumed then $A_b = \dfrac{\pi h^2}{2}$ (theory A), and if a spherical nosed cylinder is assumed then $A_b = \pi h^2$ (theory B).

The penetration height, can be said to be a characteristic of the scale of the disturbance produced by the jet. Values of the penetration heights were determined directly from the schlieren photographs, they were normalised by the diameter of the jet orifice, they were plotted as a function of the correlation parameter discussed previously and they were compared with each of the above theories (figure 7). The penetration heights predicted using theory B agree better

with the experimental findings of the blunt cone case. The experimental findings of the sharp cone agree better with those results predicted using theory A. For the sharp cone the data correlates as

$$\frac{h}{d_j} = 1.204\left[\frac{P_{oj}}{P_2 M_2^2}\right]^{0.497}$$

and for the blunt cone

$$\frac{h}{d_j} = 2.422\left[\frac{P_{oj}}{P_2 M_2^2}\right]^{0.383}$$

Both models predict the main experimental observations, 1) the jet penetration on the sharp cone is less than that of the blunt cone for the same incidence. The changes in surface pressure distribution on a conical body due to nose bluntness are well known. From pressure measurements conducted on both configurations at zero incidence, without jet, it was found that the effect of the nose bluntness is felt over the entire body length. The surface pressure distribution is reduced by the overexpansion at the shoulder to about 70 per cent of the sharp cone values. The jet pressure ratio will be greater on the blunt cone than that on the sharp cone configuration. Hence, the penetration of the jet into the undisturbed flow will be greater in the blunt cone case and 2) the penetration height of the jet is greater when the jet is on the leeward side ($\alpha + ve$) than when it is on the windward side ($\alpha - ve$). As the incidence is increasing, the correlation parameter and the jet pressure ratio are increasing, hence the penetration of the jet into the undisturbed flow will be greater when the jet is on the leeward side.

4. Pressure measurements

The resulting separation strongly alters the surface pressure distribution ahead of the jet. This effect is illustrated in the pressure measurements (figure 5). The integration of this modified pressure distribution results in a force which can be larger than the nominal jet thrust.

The separated flow region behind the jet makes a negative contribution to the control force, since near the base of the models the surface pressure was found to be consistently lower than the undisturbed cones values since the primary flow overexpands around the jet in a manner similar to that on the afterbody of a model. This overexpansion is evident in the schlieren pictures.

In the upstream centreline pressure distribution, the pressure increases on the surface of the cones to the point at which flow separates, then there is a further rise up to a pressure plateau. In the vicinity of the jet, the pressure distribution shows a drop from the plateau value (this drop can be seen only in the pressure traces of the sharp cone at - 5° incidence, and of the blunt cone at 0° incidence). After this drop, the pressure rises to a peak just ahead of the jet. The position of this peak corresponds with the location of the main reattachment ahead of the jet. This peak pressure is determined largely by the pressure at the mutual stagnation point along the dividing streamlines (assuming little mixing from the mutual stagnation point to the surface), where the two vortices meet on the cone surface.

The blunt-cone pressure results show lower plateau pressure ratios for the incidences 5, 0 and -5 degrees. It is difficult to deduce the same for the other incidences. The pressure at -10 and -15 degrees incidences shows a continuous rise, and no plateau is visible. The reduction in the plateau pressure is consistent with the effect of the reduction in the local Mach number resulting from the leading-edge bluntness.

Length of the separation region was taken as the distance from the jet nozzle to the point where the pressure on the cones acquires the undisturbed value. The separation point as determined from the pressure distributions coincides with the point of the impingement of the separation shock.

Static pressure and flow visualisation data imply that the behaviour of the flow in the vicinity of separation depends only upon the upstream conditions and is almost independent of the mechanism by which separation is produced.

FORCE MEASUREMENTS

The calculated forces and moment values were non-dimensionalised using the following equations

$$CN = \frac{N}{0.5\gamma_\infty P_\infty M_\infty^2 S_b}$$

$$CA = \frac{A}{0.5\gamma_\infty P_\infty M_\infty^2 S_b}$$

$$Cm = \frac{M}{0.5\gamma_\infty P_\infty M_\infty^2 S_b l_b}$$

The pitching moments were measured at the moment reference point located at x/d=-10.2 along the body axis.

1. Estimation of jet-only contribution

Tests, with jet only, were performed, under vacuum conditions, without running the gun tunnel. The jet thrust contributed a negative downward normal force (CN(j)=-21x10⁻³), a positive backward axial force (CA(j)=4.2x10⁻³), and a positive nose-up pitching moment (due to the jet axis being aft of the moment centre, Cm(j)=4.8x10⁻³). The jet reaction force had direction opposite to the firing of the jet.

2. Jet interaction force measurements

The tests to study the effects of the jet/crossflow interaction on the total reaction force generated by the jet were conducted by first establishing a steady jet and then firing the tunnel. The normal force history resulting from this process is shown in figure 8. The presence of the jet at t=0 produces a negative force. The magnitude of this force is constant after 100 ms due to the jet plenum chamber becoming choked.

The firing of the tunnel and the increase in pressure in the interaction region at 0° incidence augments the jet force. The completion of the tunnel run and the removal of the augmentation force results in the mean force returning to the jet force level. The increase in noise during and after the run is due to the mechanical oscillations.

3. Calculation of the axial centre of pressure

The axial centre of pressure, Xcp, was calculated by $Xcp = l_b \dfrac{Cm}{CN} + 41$, relative to the base of the cones.

4. Results

The aerodynamic coefficients measured on the cones (in absence and in the presence of the jet) are shown in figure 9. The small normal force and pitching moment coefficients measured at 0 incidence are due to the centreline focusing effect associated with imperfections in the surface of the Mach 8.2 nozzle.

The effect of mass addition to the axial force coefficient is very small at all incidences. The total induced force contributes a positive increase at every incidence, which is almost of a constant value independent of angle of attack.

The effect of the jet injection is more pronounced in the normal force coefficient. The total induced force contributes a negative increase at every incidence. That means, at positive incidences, the normal coefficient becomes less positive, and at negative incidences it becomes more negative. The effect is the shift of the normal coefficient curves to the right. By comparing the curves, it was found that this shift is of the same order, and each curve crosses the Y-axis at approximately 3° incidence.

At $\alpha = 0°$, the absolute normal force coefficient measured in the presence of the jet was CN(total)=-43x10⁻³ for the blunt cone and CN(total)=-55x10⁻³ for the sharp cone (including the normal force on the cone, CN(BluntCone)=-11x10⁻³ and CN(SharpCone)=-19x10⁻³. The combined jet and interaction normal force was therefore -32x10⁻³ for the blunt cone (52% augmentation of the total force) and -36x10⁻³ for the sharp cone (72% augmentation of the total force).

The jet increases the moment on the cones (at $\alpha = 0°$) from Cm=4x10⁻³ (in the absence of the jet) to Cm(total)=12x10⁻³ for the blunt cone, and from Cm=-1.5x10⁻³ (in the absence of the jet) to Cm(total)=7.5x10⁻³ for the sharp cone. The combined jet and interaction pitching moment for the blunt configuration is 8x10⁻³ (66% augmentation of the pitching moment) and for the sharp cone is -9x10⁻³ (87.5% augmentation of the pitching moment).

The relative locations of the centre of pressure of the jet alone and of the interaction force alone are shown in figure 10.

A forward movement of the centre of pressure was observed for positive incidences of the same order for both configurations. A rearward motion was observed at negative incidences. This migration can be understood in terms of the pressure distribution. The jet orifice is located aft the moment strain gauge (moment centre). At *negative incidences* (nose down) the main contribution towards the normal force and moment comes from the vicinity of the jet and the region behind it, (because there is a very small separated region ahead of the jet). The total force due to jet/flowfield interaction and jet thrust produces a positive contribution around the moment gauge. This causes the moment gauge to sense a less negative moment.

At *positive incidences* (nose up) the main contribution comes mainly from the upstream region, (because there is a larger separated region ahead of the jet). From the moment measurements it was found that the total induced force produces a positive contribution. This results the moment gauge to sense a more positive moment.

Satisfactory correlation of K was obtained using the correlation parameter described in a previous section (figure 11). For the sharp cone the data correlates as

$$K = 3.21 \left[\frac{P_2 M_2^{\,2}}{P_{oj}} \right]^{0.2619}$$

and for the blunt cone

$$K = 4.18 \left[\frac{P_2 M_2^{\,2}}{P_{oj}} \right]^{0.2466}$$

Smaller amplification factors were deduced for the blunt cone. This is because of the effects of bluntness on pressure distribution.

A total 50 to 160 percent augmentation of the jet thrust was calculated. Amplification factors are less for the three-dimensional flow in cones than for the two-dimensional flow on flat plates. It is believed that much of the beneficial interaction force is reduced as the high pressure regions propagate circumferentially around the body. The location of the jet near the base minimises the loss in interaction force due to spreading of the jet region of influence. This is very desirable for laminar boundary layer where the jet spreading action is more pronounced. Having the jet near the base also reduces the body area exposed to corrosive exhaust gases, which may used as the jet medium.

CONCLUSIONS

1. The introduction of nose bluntness causes delay in separation. This effect is attributed to the viscous bluntness interaction parameter.

2. As the angle of attack is increasing the separation distance is increasing. The oscillation of the bow shock ahead of the jet, it is believed to be associated with the unstable characteristics of the boundary-layer separation.

3. The penetration height values predicted using the spherical nosed cylinder model agree better with the findings from the blunt cone. On the other hand, the sharp cone findings agree with the results predicted using the quarter-half cylinder model.

4. Both models predict the main experimental observations, 1) the penetration height of the jet is increasing with increasing incidence and 2) the jet penetration height on the sharp cone is less than that on the blunt cone.

5. The pressure measurement results confirmed the findings of the schlieren pictures. The blunt-cone pressure results show lower plateau pressure ratios. The reduction in plateau pressure is consistent with the effect of the reduction in the local Mach number.

6. The ensuing interaction causes a change in surface pressure around the injector. This pressure distribution modification results in a force which is about 50 % to 160 % larger than the nominal jet thrust.

7. The presence of the jet causes a rearward motion of the axial centre of pressure at negative incidences and a forward motion at positive incidences.

REFERENCES

Brower Jr., W.. Theory, tables and data for compressible flow.

Charwat, A., Allegre, J. (1964). Interaction of a supersonic stream and a transverse supersonic jet. AIAA journal, Vol. 2, No. 11, 1965-1972.

Coet M., Delery J., Chantez B. (1992). Experiments on shockwave-boundary layer interaction at high mach number with entropy layer effect. IUTAM Symposium/Marseille, France-September, 1-4, 1992.

High, M., Blick, E. (1964). Cone pressure distribution at large and small angles of attack. AIAA Journal, Vol. 2, No. 11, 2054-2055.

Holden, M. (1975). Experimental studies of shockwave-boundary layer interaction. AGARD AG-203.

Opatowski, T. (1968). A three component gun tunnel balance designed for testing thin delta wings. ARC 31-278.

Simpkins, P. (1968). Hypersonic interactions about a slender cone induced by radial mass injection. AGARD CP-30.

Taylor, G. (1954). Scientific Papers 3, 537-540 ed. G. Batchelor. Cambridge University Press.

Townsend, J. (1965). Effects of leading-edge bluntness and ramp deflection angle on laminar boundary-layer separation in hypersonic flow. NASA TN D-3290.

Trimmer, L. (1966). Equations and charts for evaluation of forces on spherically blunted cones by the newtonian theory. AEDC TR-66-16.

Van Hise, V. (1961). Analytic study of induced pressure on long bodies of revolution with varying nose bluntness at hypersonic speeds. NASA TR R-78.

Vermeulen, J., Simeonides, G. (1992). Parametric study of shockwave/boundary layer interactions over 2-D compression corners at Mach number 6. VKI TN-181

Wells, W., Armstrong, W. (1961). Tables of aerodynamic coefficients obtained from developed newtonian expressions for complete and partial conic and spheric bodies at combined angles of attack and sideslip with some comparisons with hypersonic experimental data. NASA TR R-127.

Zukoski, E., Spaid, F. (1964). Secondary injection of gases into a supersonic flow. AIAA Journal, Vol. 2, No. 8, 1689-1696.

FIGURES
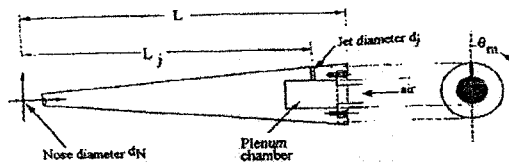
Figure 1 General structure of the cone model

a) schlieren picture
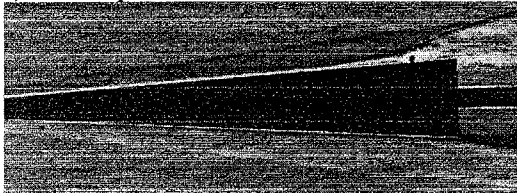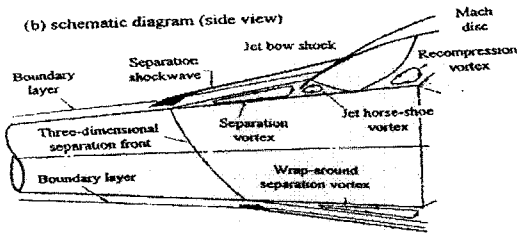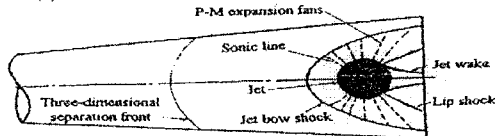
Figure 2 General structure of the interaction region (sharp cone, $\alpha = 0^{\circ}$)
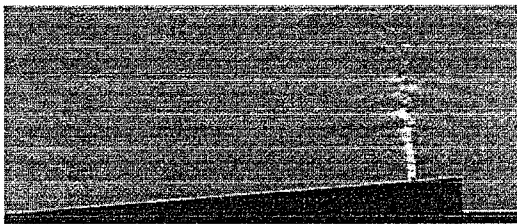
Figure 3a Structure of the jet only
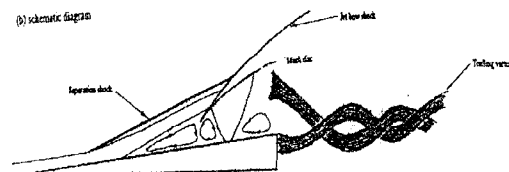
Figure 3b Trailing vortex structures

11
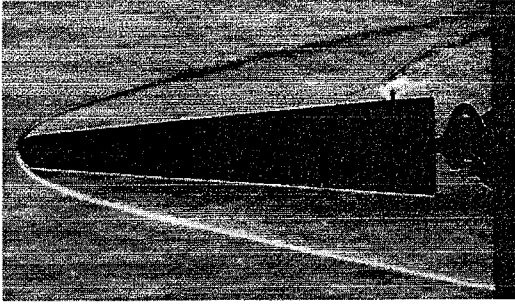
$\alpha = 0^o$, blunt cone

$\alpha = 1 0^o$, sharp cone
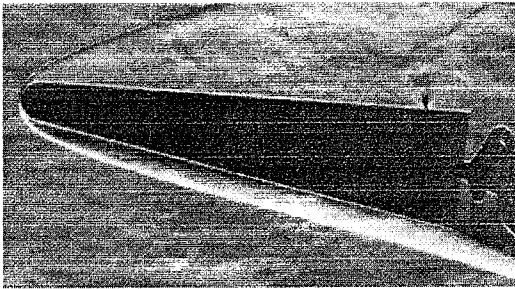
blunt cone

$\alpha = -1 0^o$, sharp cone
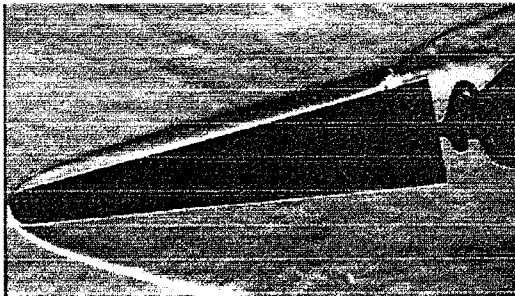
blunt cone

Figure 4 Effect of bluntness and incidence on the flowfield characteristics

a) blunt cone
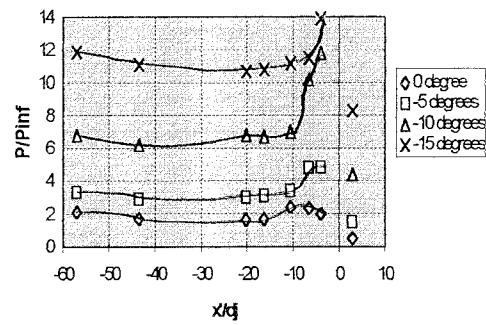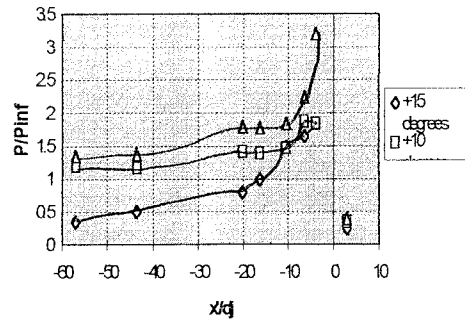
b) sharp cone
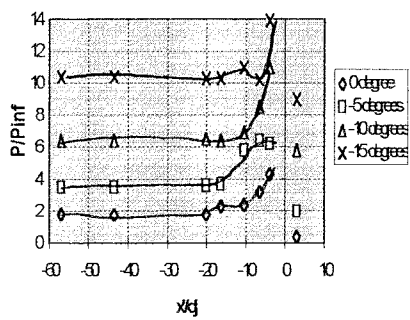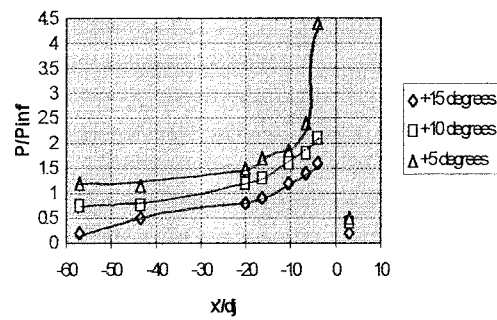
Figure 5 Pressure measurements
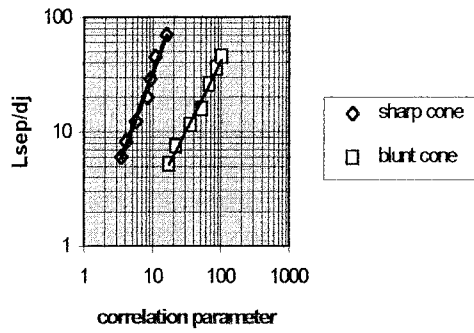
Figure 6 Correlation of the separated flow length

a) blunt cone
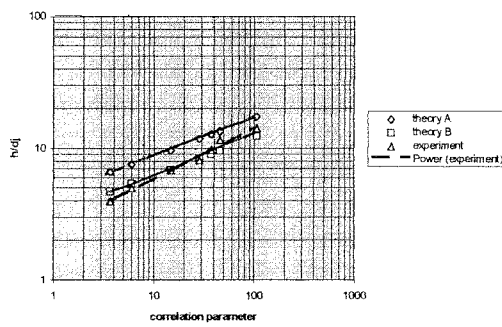
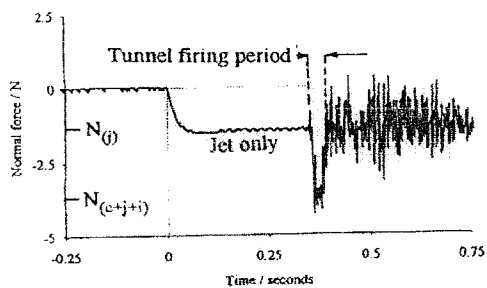b) sharp cone
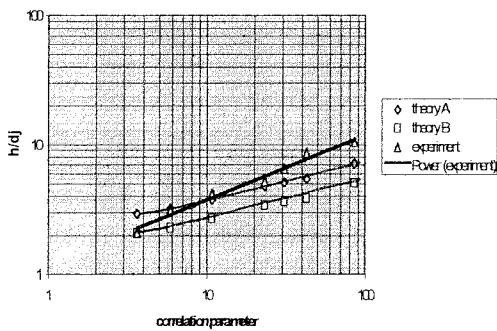
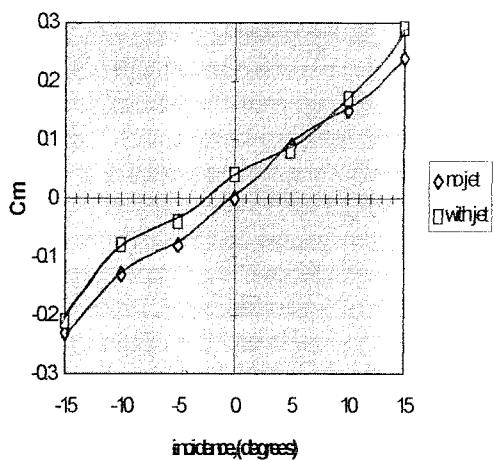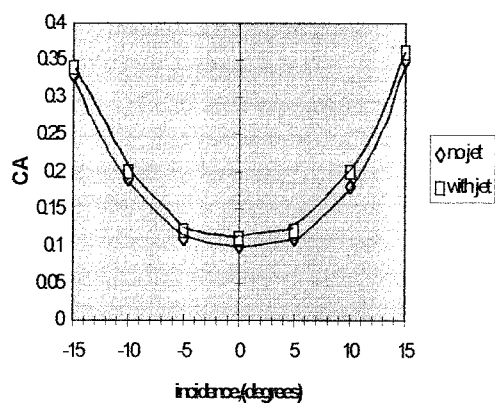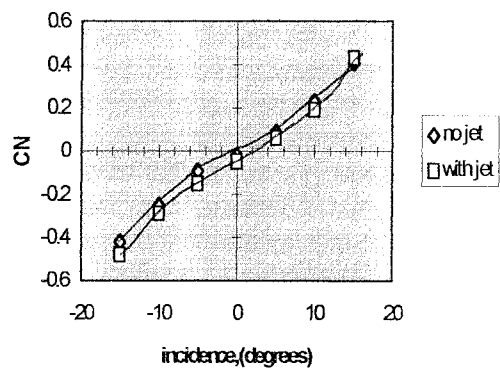
Figure 7 Comparison of jet penetration heights with theory

Figure 8 The effects of the jet and the jet/crossflow interaction on normal force
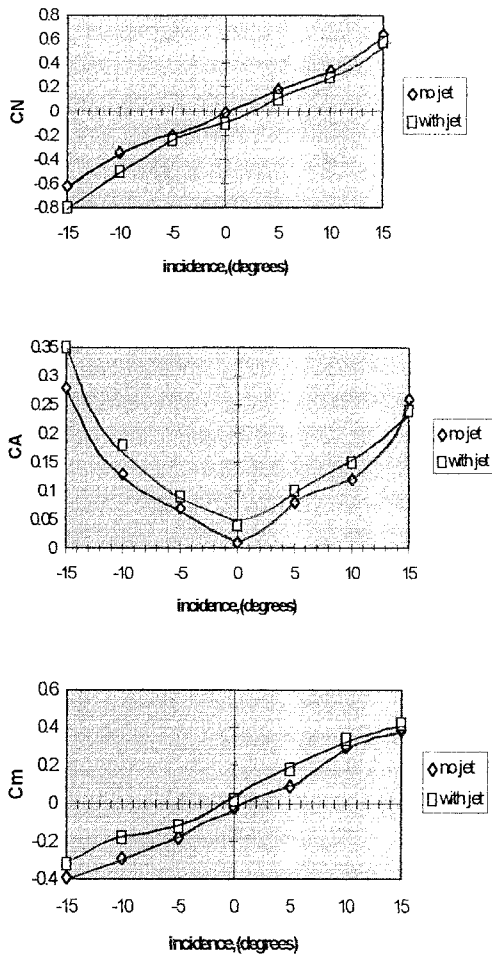
a) blunt cone

b) sharp cone

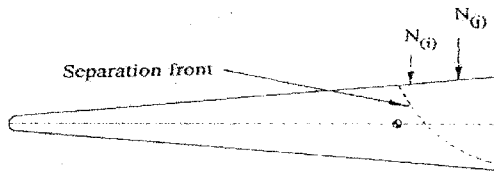Figure 9 The aerodynamic coefficients in the absence and in the presence of the jet

Figure 10 The relative locations of the centre of pressure of the jet and the interaction force (blunt cone, $\alpha = 0^o$)
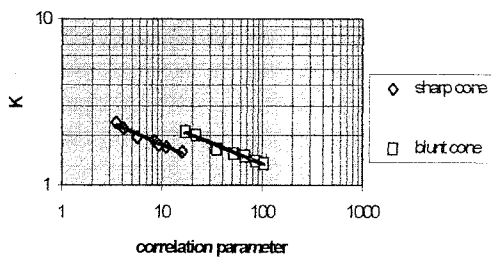

Figure 11 Amplification factor dependance on the correlation parameter